Photoacoustic Molecular Imaging using Single Walled Carbon Nanotubes in Living Mice

Adam de la Zerda[1,2], Cristina Zavaleta[1], Shay Keren[1], Srikant Vaithilingam[2], Sunil Bodapati[1], Robert Teed[1], Zhuang Liu[3], Jelena Levi[1], Bryan R. Smith[1], Te-Jen Ma[2], Omer Oralkan[2], Zhen Cheng[1], Xiaoyuan Chen[1], Hongjie Dai[3], Butrus T. Khuri-Yakub[2], Sanjiv S. Gambhir[1,4]

[1]Molecular Imaging Program at Stanford, Department of Radiology and Bio-X Program, the [2]Department of Electrical Engineering, the [3]Department of Chemistry and the [4]Department of Bioengineering, Stanford University, Palo Alto, CA 94305, USA.

ABSTRACT

Photoacoustic molecular imaging is an emerging technology offering non-invasive high resolution imaging of the molecular expressions of a disease using a photoacoustic imaging agent. Here we demonstrate for the first time the utility of single walled carbon nanotubes (SWNTs) as targeted imaging agents in living mice bearing tumor xenografts. SWNTs were conjugated with polyethylene-glycol-5000 connected to Arg-Gly-Asp (RGD) peptide to target the $\alpha_v\beta_3$ integrin that is associated with tumor angiogenesis. In-vitro, we characterized the photoacoustic spectra of the particles, their signal linearity and tested their uptake by $\alpha_v\beta_3$-expressing cells (U87MG). The photoacoustic signal of SWNTs was found not to be affected by the RGD conjugation to the SWNTs and was also found to be highly linear with concentration ($R^2 = 0.9997$ for 25-400nM). The cell uptake studies showed that RGD-targeted SWNTs gave 75% higher photoacoustic signal than non-targeted SWNTs when incubated with U87MG cells. In-vivo, we measured the minimal detectable concentration of SWNTs in living mice by subcutaneously injecting SWNTs at increasing concentrations. The lowest detectable concentration of SWNTs in living mice was found to be 50nM. Finally, we administered RGD-targeted and non-targeted SWNTs via the tail-vein to U87MG tumor-bearing mice (n=4 for each group) and measured the signal from the tumor before and up to 4 hours post-injection. At 4 hours post-injection, tumors of mice injected with RGD-targeted SWNTs showed 8 times higher photoacoustic signal compared with mice injected with non-targeted SWNTs. These results were verified ex-vivo using a Raman microscope that is sensitive to the SWNTs Raman signal.

Contact information: sgambhir@stanford.edu

INTRODUCTION

Photoacoustic imaging is an emerging imaging modality that overcomes, to a great extent, the resolution and depth limitations of optical imaging but maintains the high-contrast of optics[1-7].

Photons Plus Ultrasound: Imaging and Sensing 2009, edited by Alexander A. Oraevsky, Lihong V. Wang,
Proc. of SPIE Vol. 7177, 717725 · © 2009 SPIE · CCC code: 1605-7422/09/$18 · doi: 10.1117/12.806497

When a short light pulse is used to illuminate tissues, the light is scattered and absorbed as it propagates through the tissues. The absorbed light is converted into heat, which in return causes the material to locally expand, creating a pressure wave. The pressure wave can then be detected by an ultrasound system placed outside the subject of interest. By measuring the pressure waves from several positions, a full tomographic image can be reconstructed. However, many diseases, especially in their early stages, do not exhibit a natural photoacoustic contrast, therefore administering an external photoacoustic contrast agent is necessary. While a number of contrast agents for photoacoustic imaging have been suggested previously[8-15], most were not shown to target a diseased site in living subjects. The ideal molecular imaging agent will have a sufficiently large optical absorption cross section to maximize the agent's photoacoustic signal, but yet be small enough to escape uptake by the reticuloendothelial system (RES), specifically the liver and the spleen. However, designing such an imaging agent is not trivial since a particle's absorption cross section and its size are highly correlated.

In this study, single walled carbon nanotubes (SWNTs) were shown to have utility as photoacoustic contrast agents. Since SWNTs are essentially folded single layers of graphite, which have strong light absorption characteristics, they may act as photoacoustic contrast agents. SWNTs can be made as small as 1 nm in diameter but yet their length can extend to hundreds of nanometers increasing their absorption cross section and their intrinsic photoacoustic contrast. This unique geometry of SWNTs led to several applications of SWNTS in nanomedicine including drug delivery[16] and photothermal therapy[17]. However, in order to successfully translate these emerging applications into practice, it is essential to non-invasively monitor the physical location of the SWNTS in the subject of interest[18]. To monitor SWNTs in living subjects, previous studies attached reporting molecules (fluorophores[19] or radioactive isotopes[20]) to the nanotube's surface. Conversely, photoacoustic imaging of SWNTs does not require attaching any additional reporting molecules on the nanotubes and can produce three dimensional images with much higher spatial resolution and high depth penetration.

1. METHODS AND MATERIALS

SWNT conjugates synthesis. A complete description of the synthesis of SWNT-RGD and plain SWNT can be found elsewhere[20]. The SWNTs used in this work were 50-300 nm in length and 1-2 nm in diameter and have an average molar weight[21] of 170 kDa per SWNT (based on 150 nm length and 1.2 nm diameter). were coupled to the RGD peptides through polyethylene glycol-5000 grafted phospholipid (PL-PEG_{5000}). These SWNT-RGD conjugates bind with high affinity to $\alpha_v\beta_3$ integrin that is over-expressed in tumor neovasculature as well as to other integrins expressed by tumors but with lower affinity[22, 23]. We also synthesized non-targeted SWNTs by conjugating them solely to PL-PEG_{5000} (plain SWNT) (**Fig. 1**).

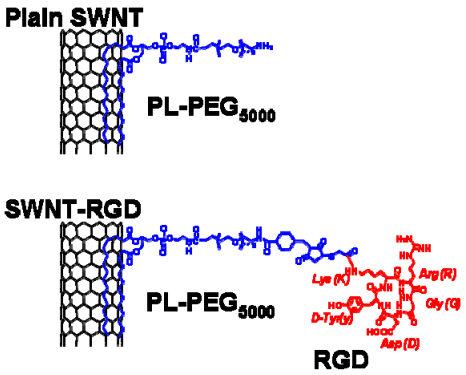

Figure 1 - Illustration of plain SWNT and SWNT-RGD. The phospholipid (PL) binds to the sidewall of the SWNT connecting the polyethylene glycol-5000 (PEG_{5000}) to the SWNT. The RGD allows the SWNT to bind to tumor integrins such as $\alpha_v\beta_3$.

Photoacoustic imaging instrument. Our photoacoustic system[24] is illustrated in **Fig. 2**. A tunable pulsed laser with a repetition rate of 10 Hz and a pulse width of 5 ns (Nd:YAG Surelight-III-10 connected to Surelite OPO Plus, Continuum) illuminated the object through a fiber optic ring light (50-1353 Ringlight, Fiberoptic Systems Inc.). The average energy density of the laser at 690 nm wavelength was measured to be ~9 mJ/cm^2 at the target site, which is below the ANSI limitation for laser skin exposure[25]. A 5 MHz focused transducer (25.5 mm focal length, 4 MHz bandwidth, F number of 2.0, depth of focus of 6.5 mm, lateral resolution of 600 μm, and axial resolution of 380 μm. A309S-SU-F-24.5-MM-PTF, Panametrics) was used to acquire both pulse-echo and photoacoustic images. In addition, high resolution ultrasound images were acquired using a 25 MHz focused transducer (27 mm focal length, 12 MHz bandwidth, F number of 4.2, depth of focus of 7.5 mm, lateral resolution of 250 μm, and axial resolution of 124 μm. V324-SU-25.5-MM, Panametrics). A precision xyz-stage (U500, Aerotech Inc.) with minimum step

size of 1μm was used to move the transducer and the fiber ring along a planar 2D trajectory. At every position, the acquired signal was averaged over 16 laser pulses. The time of arrival and the intensity of the laser pulses were recorded using a silicon photodiode (DET10A, Thorlabs). This information was used to synchronize the acquisition and compensate for pulse-to-pulse variations in laser intensity. The analog photoacoustic signals were amplified using a 40 dB preamplifier (5676/115VAC, Panametrics) and digitized using an oscilloscope (Infiniium 54825A, Agilent). The photoacoustic and ultrasound images were reconstructed as follows: the a-scan from each position of the transducer was band pass filtered with 100% fractional bandwidth, compensated for laser intensity variation and envelope detected. The a-scans were then combined to reconstruct a 3D intensity image of the target. No further post-processing was done on the images. The ultrasound images acquired using the 5 MHz and 25 MHz transducers were aligned together using small vertical translations so that the object's skin level matches in both images. Then, photoacoustic and the high frequency ultrasound images were analyzed, co-registered and displayed using AMIDE[26] software.

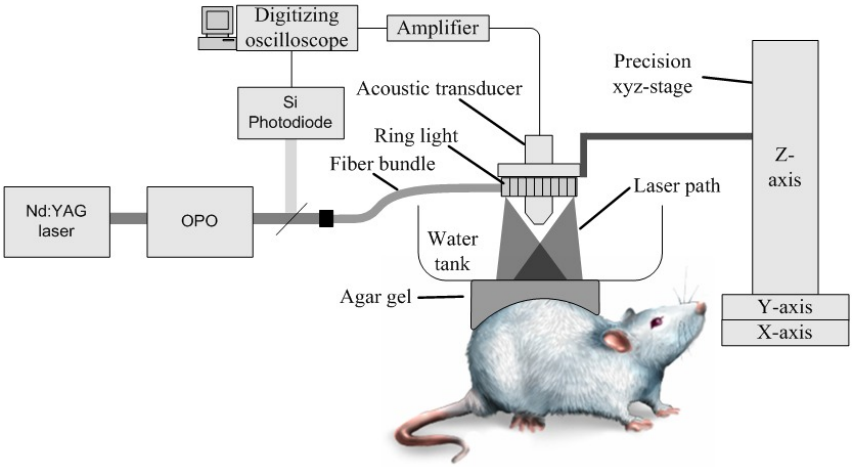

Figure 2 Photoacoustic imaging instrument. A tunable pulsed laser (Nd:YAG laser and OPO) illuminated the subject through a fiber optic ring light. The photoacoustic signals produced by the sample were acquired using a 5 MHz focused transducer. A precision xyz-stage was used to move the transducer and the fiber ring along a planar 2D trajectory. The time of arrival and the intensity of the laser pulses were recorded using a silicon photodiode. This information was used to synchronize the acquisition and compensate for pulse-to-pulse variations in laser intensity. The analog photoacoustic signals were amplified using a 40 dB preamplifier and digitized using an oscilloscope.

Animal experiments. All animal experiments were performed in compliance with the Guidelines for the Care and Use of Research Animals established by the Stanford University

Animal Studies Committee. For the tumor targeting experiments, female nude mice (n = 4 in each group) 6-8 weeks old were inoculated subcutaneously at their lower right back with 10^7 U87MG cells (American Type Culture Collection, ATCC) suspended in 50 μl of saline (PBS pH 7.4 1X, Invitrogen). The tumors were allowed to grow to a volume of ~100 mm^3. The SWNTs were sonicated for 5 min under 1 W RMS (Sonifier 150, Branson) to separate SWNTs that may have aggregated. The mice were then injected with 200μl of 1.2μM SWNTs into the tail-vein. During the injection the mice positioning was not changed. At 4 hr post-injection, the mice were sacrificed and their tumors were surgically removed for further *ex-vivo* analysis. The ultrasound images from the different time points were aligned to one another, by vertically translating the images (translation was typically less than 0.5 mm). The same alignment was then applied to the photoacoustic images.

2. RESULTS

Characterization of SWNT photoacoustic properties. In a phantom study we measured the photoacoustic signal of plain SWNT and SWNT-RGD at wavelengths of 690-800 nm (**Fig. 3a**) (shorter wavelengths are less desirable as the depth of penetration through the tissues is reduced[27]). These photoacoustic spectra suggested that 690 nm is the preferable wavelength since the SWNTs photoacoustic signal is highest. Furthermore, the ratio of SWNTs to hemoglobin signal is higher at this wavelength as compared to other wavelengths. Importantly, the photoacoustic signal of SWNTs was found to be unaffected by the RGD peptide conjugation. In a separate non-absorbing and non-scattering phantom study, we also validated that the photoacoustic signal produced by SWNTs is linear to their concentration (**Fig. 3b**) with R^2 = 0.9997.

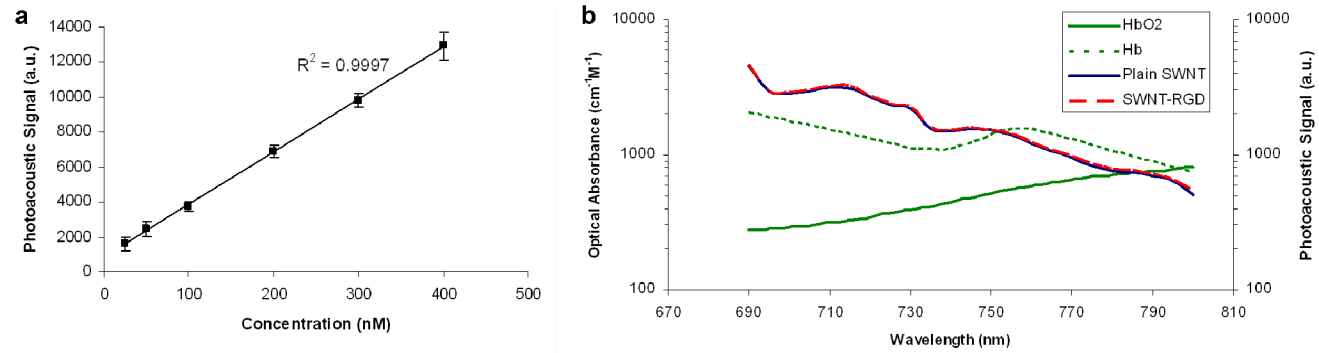

Figure 3 - Characterization of SWNT photoacoustic properties. a, The photoacoustic signal produced by SWNTs was observed to be linearly dependent on the concentration (R^2 = 0.9997). **b,** The photoacoustic spectra of plain SWNT (blue) and SWNT-RGD (dotted red) are overlaid on the known optical absorbance of HbO2 (green) and Hb (dotted green). The spectral overlap between plain SWNT and SWNT-RGD suggests that the RGD conjugation does not perturb their photoacoustic signal.

Cell uptake studies. We exposed SWNT-RGD to U87MG cells that express $\alpha_v\beta_3$ integrin on their surface for 30 min. Control studies included U87MG cells exposed to either plain SWNT or saline and HT-29 cells, which do not express $\alpha_v\beta_3$ integrin on their surface, exposed to SWNT-RGD. After exposure, the cells were washed with saline to remove unbound SWNTs and scanned *ex-vivo* using a Raman microscope. SWNTs produce a very unique Raman signal[28], allowing a Raman microscope to detect low concentrations of SWNTs in cells. U87MG cells that were exposed to SWNT-RGD were found to have 75% higher signal than U87MG cells exposed to plain SWNT ($p < 0.05$) and 195% higher signal than HT-29 cells exposed to SWNT-RGD ($p < 0.05$). Cells exposed to saline only showed negligible signal compared to any of the groups ($p < 0.05$) (**Fig. 4**).

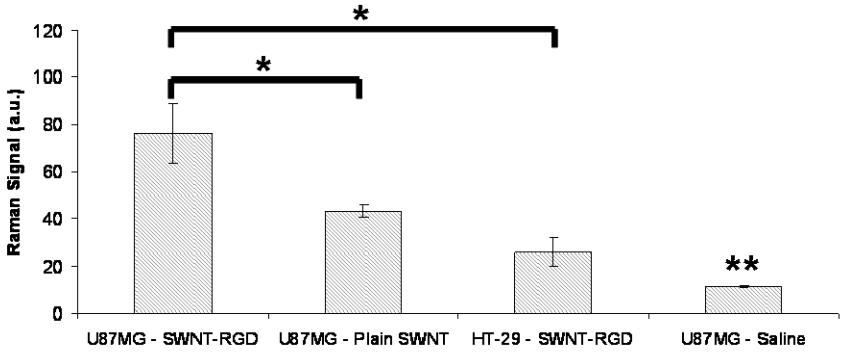

Figure 4 – SWNT cell uptake studies. U87MG incubated with SWNT-RGD showed 75% higher SWNT signal than control U87MG cells which were incubated with plain SWNT and 195% higher SWNT signal than HT-29 cells which were incubated with SWNT-RGD. " * " indicates $p < 0.05$. U87MG cells

incubated with saline only showed significantly lower signal than all groups ("*" indicates $p < 0.05$ compared to all other groups on the graph).

Photoacoustic detection of SWNTs in living mice. We then injected the lower back of a mouse subcutaneously (under the skin) with 30 µl of SWNTs-matrigel mixtures at concentrations between 50 to 600 nM (n = 3 for each concentration). Matrigel alone produced no photoacoustic signal (data not shown). Upon injection, the matrigel solidified, fixing the SWNTs in place and three-dimensional (3D) ultrasound and photoacoustic images of the inclusions were acquired (**Fig. 5a**). While the ultrasound images showed the mouse anatomy (e.g., skin and inclusion edges), the photoacoustic images revealed the SWNTs contrast in the mouse. The photoacoustic signal from each inclusion was quantified using a three dimensional region of interest (ROI) drawn over the inclusion. We observed a linear correlation ($R^2 = 0.9929$) between the SWNTs concentration and the corresponding photoacoustic signal (**Fig. 5b**). We concluded that the photoacoustic signal produced by tissues (background) was equivalent to the photoacoustic signal produced by 50 nM of SWNTs (i.e., signal to background ratio = 1).

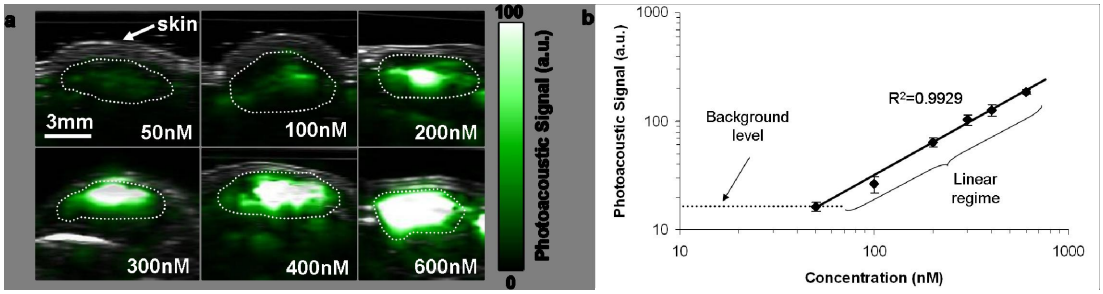

Figure 5 - Photoacoustic detection of SWNTs in living mice. a, Mice were injected subcutaneously with SWNTs at concentrations 50-600 nM. One vertical slice in the 3D photoacoustic image (green) was overlaid on the corresponding slice in the ultrasound image (gray). The skin is illustrated in the ultrasound images, while the photoacoustic images show the SWNTs. The dotted lines on the images illustrate the edges of each inclusion. **b,** The photoacoustic signal from each inclusion was calculated and the 'background level' represents the endogenous signal measured from tissues. The error bars represent standard error (n = 3). The linear regression is calculated on the five most concentrated inclusions ($R^2 = 0.9929$).

SWNT tumor targeting in living mice. We then injected two groups of mice, bearing U87MG tumor xenografts (~100 mm^3) via the tail-vein (IV) with either 200 µl of plain SWNT (n = 4) or SWNT-RGD (n = 4) at a concentration of 1.2 µM. 3D ultrasound and photoacoustic images of the tumor and its surroundings were acquired before and up to 4 hr after injection. We found that

mice injected with SWNT-RGD showed a significant increase of photoacoustic signal in the tumor compared to control mice injected with plain SWNT (**Fig. 6a**). The images from the different time points were aligned with one another using simple vertical translations to account for small vertical movements in the transducer positioning. This alignment allowed quantification of the photoacoustic signal at all time points using a single ROI. We then calculated a subtraction image between the photoacoustic image taken at 4 hr post-injection and the photoacoustic image taken pre-injection. The subtraction image better visualize the real SWNTs distribution as it removes, to a large extent, the background signal. For example, in the mouse injected with plain SWNT (**Fig. 6a**), a high photoacoustic signal, likely produced by a large blood vessel, was seen in the pre-injection and post-injection images. However, the subtraction image showed much lower signal from this area, reflecting the likely low concentration of plain SWNT there. We calculated the photoacoustic signal by drawing a 3D ROI around the tumor (tumor boundaries were clearly visualized in the ultrasound images). The photoacoustic signal increase was quantified as a function of time (**Fig. 6b**). While SWNT-RGD led to a consistently higher photoacoustic signal, plain SWNT led only to a temporary increase in the photoacoustic signal of the tumor ($p < 0.001$ for comparing the entire time-curves, and $p < 0.05$ for comparing the signals at each time-point independently). The temporary photoacoustic signal observed by plain SWNT is likely caused by circulating SWNTs that are eventually cleared from the blood stream. Conversely, SWNT-RGD bind to the tumor vasculature creating a consistent photoacoustic signal from the tumor. On average, at 4 hr post-injection, SWNT-RGD led to ~8 times higher photoacoustic signal increase compared to plain SWNT.

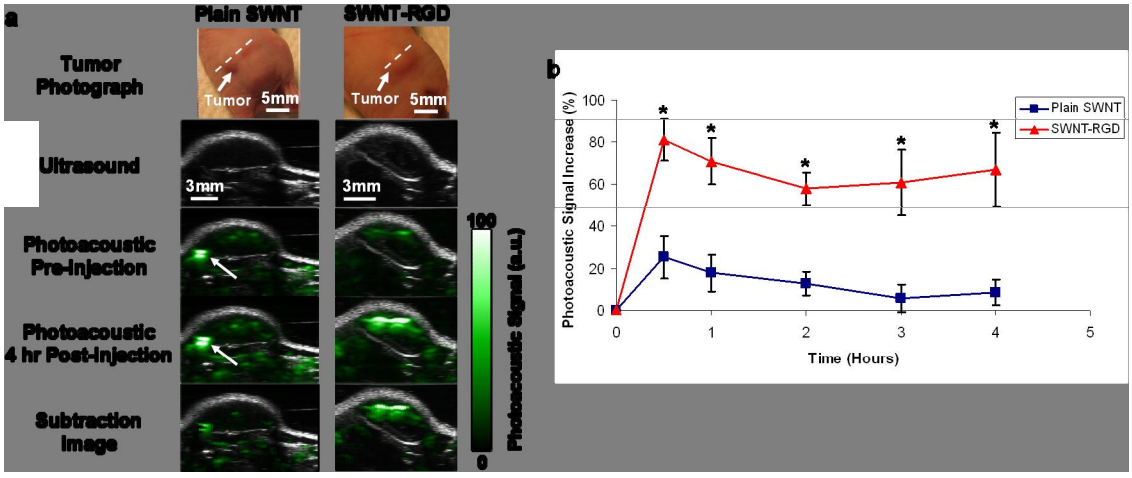

Figure 6 - SWNT targets tumor in living mice. a, Ultrasound (gray) and photoacoustic (green) images of one vertical slice (white dotted line) through the tumor. The ultrasound images show the skin and the tumor boundaries. Subtraction images were calculated as 4 hr post-injection minus pre-injection. The high photoacoustic signal in the mouse injected with plain SWNTs (indicated with white arrow) is not seen in the subtraction image, suggesting that it is due to a large blood vessel and not SWNTs. **b,** Mice injected with SWNT-RGD showed a significantly higher photoacoustic signal than mice injected with plain SWNT ($p < 0.001$). The error bars represent standard error ($n = 4$). " * " denotes where $p < 0.05$.

We further validated our photoacoustic results using a Raman microscope, as an independent method for detection of SWNTs. At the conclusion of the photoacoustic study, 4 hr post-injection, the mice were sacrificed; the tumors were surgically removed and scanned *ex-vivo* under a Raman microscope. The 2D Raman images of the excised tumors were found to match the photoacoustic images (**Fig. 7a**). The mean Raman signal from the tumors was calculated from the Raman images. Similarly to the photoacoustic results, the Raman signal from the tumors was ~4 times higher in mice injected with SWNT-RGD compared to mice injected with plain SWNT (**Fig. 7b**).

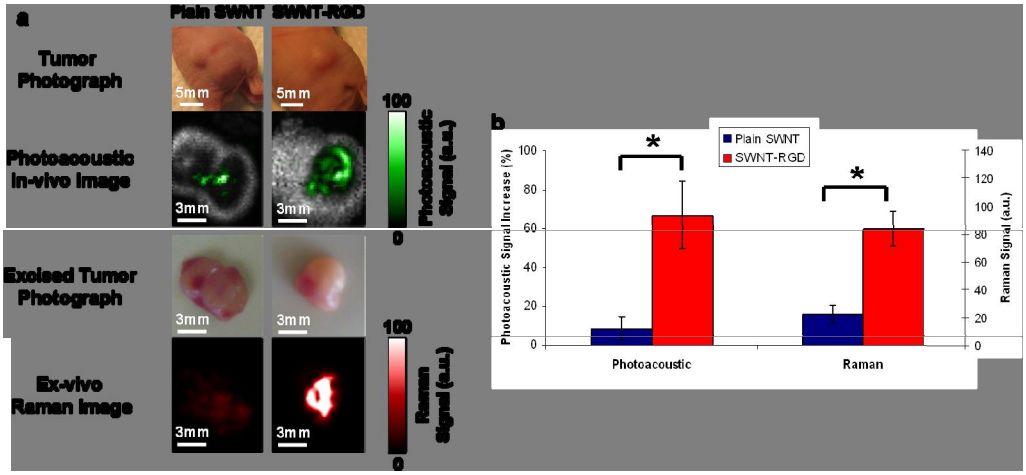

Figure 7 Validation of the *in-vivo* photoacoustic images by *ex-vivo* Raman microscopy. a, Photographs of the tumors in mice and the corresponding photoacoustic subtraction images shown as horizontal slices through the tumors. After the photoacoustic scan, the tumors were excised and scanned using a Raman microscope (red). Mice injected with plain SWNT (left column) showed both low photoacoustic and Raman signals compared to mice injected with SWNT-RGD (right column). The tumors are in the same orientation in all images. **b,** Comparison between the photoacoustic signal of the tumors *in-vivo* (left axis) and the Raman signal acquired from the excised tumors (right axis). " * " denotes where $p < 0.05$.

3. DISCUSSION AND CONCLUSION

We have demonstrated that SWNTs can be exploited as photoacoustic contrast agents to non-invasively image tumors. Intravenous injection of targeted SWNTs in mice led to 8 times higher photoacoustic signal in the tumor compared to mice injected with non-targeted SWNTs. Our photoacoustic images were verified using Raman microscopy on the surgically removed tumors. Furthermore, our results agreed with a previous study[20] where radiolabeled SWNT-RGD were monitored using small animal positron emission tomography (microPET). In that study, SWNT-RGD were found to accumulate ~3-5 times more in tumors than plain SWNT. That study also showed that the SWNT-RGD did not accumulate in the tissue surrounding the tumor.

Most previous work on photoacoustic contrast agents *in-vivo* is limited to non-targeted agents such as gold nanocages used for highlighting the blood vessels in a rat's brain[11]. Various gold nanoparticles have been previously suggested primarily for their high absorption characteristics and the ability to control their spectra allowing multiplexing studies[9]. However, their main limitation is their relatively large size, which will lead to their rapid clearance by the reticuloendothelial system (RES) upon intravenous injection. It is possible that SWNTs, due to their unique high aspect ratio (~1:100) and high surface area to volume ratio, are capable of minimizing RES uptake while having an increased affinity for molecular targets due to multivalency effects[20]. With respect to acquisition time, our current instrument acquires a single photoacoustic image in ~20-30 min for a tumor approximately 100 mm^3 in size. However, by using lasers with higher repetition rates, scan duration can be greatly reduced.

While SWNTs have the capability to efficiently bind to molecular targets, their high photoacoustic signal allows for high resolution 3D photoacoustic images with substantial depth of penetration. None of the other molecular imaging modalities compares with the precise depth information and sub-millimeter resolution at nano-molar sensitivity that is achieved by photoacoustic imaging.

ACKNOWLEDGEMENTS

We would like to thank Jarrett Rosenberg for the statistical analysis. This work was supported, in part, by NCI CCNE U54 (SSG) and NCI ICMIC P50 CA114747 (SSG).

REFERENCES

1. Xu, M.H. & Wang, L.H.V. Photoacoustic imaging in biomedicine. *Rev. Sci. Instrum.* **77**, 041101-043100 (2006).

2. Oh, J.T. et al. Three-dimensional imaging of skin melanoma in vivo by dual-wavelength photoacoustic microscopy. *J. Biomed. Opt.* **11**, 34032 (2006).
3. Zhang, H.F., Maslov, K., Stoica, G. & Wang, L.V. Imaging acute thermal burns by photoacoustic microscopy. *J. Biomed. Opt.* **11**, 054033 (2006).
4. Wang, X., Xie, X., Ku, G., Wang, L.V. & Stoica, G. Noninvasive imaging of hemoglobin concentration and oxygenation in the rat brain using high-resolution photoacoustic tomography. *J. Biomed. Opt.* **11**, 024015 (2006).
5. Zhang, H.F., Maslov, K., Stoica, G. & Wang, L.V. Functional photoacoustic microscopy for high-resolution and noninvasive in vivo imaging. *Nat. Biotechnol.* **24**, 848-51 (2006).
6. Manohar, S. et al. Initial results of in vivo non-invasive cancer imaging in the human breast using near-infrared photoacoustics. *Opt. Express* **15**, 12277-12285 (2007).
7. Ermilov, S. et al. Detection and noninvasive diagnostics of breast cancer with 2-color laser optoacoustic imaging system *Proc. SPIE* **6437** (2007).
8. Eghtedari, M. et al. High sensitivity of in vivo detection of gold nanorods using a laser optoacoustic imaging system. *Nano Lett.* **7**, 1914-8 (2007).
9. Li, P.C. et al. Photoacoustic imaging of multiple targets using gold nanorods. *IEEE Trans. Ultrason. Ferroelectr. Freq. Control* **54**, 1642-7 (2007).
10. Kim, G. et al. Indocyanine-green-embedded PEBBLEs as a contrast agent for photoacoustic imaging. *J. Biomed. Opt.* **12**, 044020 (2007).
11. Yang, X., Skrabalak, S.E., Li, Z.Y., Xia, Y. & Wang, L.V. Photoacoustic tomography of a rat cerebral cortex in vivo with au nanocages as an optical contrast agent. *Nano Lett.* **7**, 3798-802 (2007).
12. Zharov, V.P. et al. Photoacoustic flow cytometry: principle and application for real-time detection of circulating single nanoparticles, pathogens, and contrast dyes in vivo. *J. Biomed. Opt.* **12**, 051503 (2007).
13. Meng-Lin, L. et al. Simultaneous Molecular and Hypoxia Imaging of Brain Tumors In Vivo Using Spectroscopic Photoacoustic Tomography. *Proc. of IEEE* **96**, 481-489 (2008).
14. Wei, C.-W. et al. In vivo photoacoustic imaging with multiple selective targeting using bioconjugated gold nanorods *Proc. SPIE* **6856** (2008).
15. Kim, K. et al. In vivo imaging of inflammatory responses by photoacoustics using cell-targeted gold nanorods (GNR) as contrast agent *Proc. SPIE* **6856** (2008).
16. Liu, Z., Sun, X., Nakayama-Ratchford, N. & Dai, H. Supramolecular Chemistry on Water-Soluble Carbon Nanotubes for Drug Loading and Delivery. *ACS Nano.* **1**, 50-56 (2007).
17. Son, S.J., Bai, X. & Lee, S.B. Inorganic hollow nanoparticles and nanotubes in nanomedicine Part 2: Imaging, diagnostic, and therapeutic applications. *Drug Discov. Today* **12**, 657-63 (2007).
18. de la Zerda, A. & Gambhir, S.S. Drug delivery: Keeping tabs on nanocarriers. *Nat. Nano.* **2**, 745-746 (2007).
19. Shi, D. et al. Quantum-Dot-Activated Luminescent Carbon Nanotubes via a Nano Scale Surface Functionalization for *in vivo* Imaging. *Adv. Mater.* **19**, 4033-4037 (2007).
20. Liu, Z. et al. In vivo biodistribution and highly efficient tumor targeting of carbon nanotubes in mice. *Nat. Nano.* **2**, 47-52 (2007).

21. Kam, N.W., O'Connell, M., Wisdom, J.A. & Dai, H. Carbon nanotubes as multifunctional biological transporters and near-infrared agents for selective cancer cell destruction. *Proc. Natl. Acad. Sci. U. S. A.* **102**, 11600-5 (2005).
22. Mizejewski, G.J. Role of integrins in cancer: survey of expression patterns. *Proc. Soc. Exp. Biol. Med.* **222**, 124-38 (1999).
23. Janssen, M.L. et al. Tumor targeting with radiolabeled alpha(v)beta(3) integrin binding peptides in a nude mouse model. *Cancer Res.* **62**, 6146-51 (2002).
24. Vaithilingam, S. et al. in Ultrasonics Symposium, 2007. IEEE 2413-2416 (2007).
25. American National Standards Institute, American national standard for the safe use of lasers, *ANSI Standard Z136.1-2000*, ANSI, Inc., New York. (2000).
26. Loening, A.M. & Gambhir, S.S. AMIDE: a free software tool for multimodality medical image analysis. *Mol. Imaging* **2**, 131-7 (2003).
27. Weissleder, R. & Ntziachristos, V. Shedding light onto live molecular targets. *Nat. Med.* **9**, 123-8 (2003).
28. Jorio, A., Saito, R., Dresselhaus, G. & Dresselhaus, M.S. Determination of nanotubes properties by Raman spectroscopy. *Philos. Transact. A Math. Phys. Eng. Sci.* **362**, 2311-36 (2004).
29. Schipper, M.L. et al. A pilot toxicology study of single-walled carbon nanotubes in a small sample of mice. *Nat. Nano.* **3**, 216-221 (2008).